

# A Heavy-Duty Platform for Autonomous Navigation in Kiwifruit Orchards

Mark H. Jones<sup>a,\*</sup>, Jamie Bell<sup>b,\*\*</sup>, Daniel Dredge<sup>a</sup>, Matthew Seabright<sup>a</sup>,  
Alistair Scarfe<sup>c</sup>, Mike Duke<sup>a</sup>, Bruce MacDonald<sup>b</sup>

<sup>a</sup>*School of Engineering, University of Waikato, Hamilton, New Zealand*

<sup>b</sup>*Faculty of Engineering, University of Auckland, Auckland, New Zealand*

<sup>c</sup>*Robotics Plus Ltd, Neunham Innovation Park, Tauranga, New Zealand*

---

## Abstract

Horticultural robots designed for in-field use generally require a means of transport around farms or orchards. A common approach is to directly integrate a drive system at the expense of increasing overall complexity. Alternatively, robots can be modularised and attached to general purpose platforms. General purpose platforms reported previously are designed to carry relatively light payloads orientated toward ground based crops. This paper presents a modularised platform capable of carrying modules of up to 1000 kg beneath 1.4 m high pergola-style kiwifruit canopies. The electrical and software architecture is discussed as well as vehicle's mechanical design. Sensors suitable for autonomous navigation are evaluated in-orchard and tested with prototype navigation algorithms. It is found that GNSS based navigation is not feasible under kiwifruit canopies, but perception based navigation sees the platform complete a number of block traversals autonomously.

*Keywords:* Agricultural automation, autonomous navigation, sensor selection

---

## <sup>1</sup> 1. Introduction

- <sup>2</sup> Short-term labour requirements within New Zealand's kiwifruit industry  
<sup>3</sup> peak twice a year corresponding with the pollination and harvesting of ki-  
<sup>4</sup> wifruit. The majority of employment during these peaks is filled by seasonal

---

\*markhedleyjones@gmail.com

\*\*jamie977@gmail.com

5 or casual workers (Timmings, 2009). As kiwifruit is the country's largest  
6 horticultural export by value (Statistics New Zealand, 2015), effective au-  
7 tomation in this industry will promote economic growth. Development of an  
8 automated kiwifruit harvester with integrated drive system has previously  
9 been published (Scarfe, 2012). That work presented a platform designed  
10 to autonomously navigate though pergola-style kiwifruit orchards and had  
11 four integrated harvesting arms. Work presented here focuses on creating  
12 a platform that operates independently from orchard related tasks, such as  
13 fruit harvesting and pollination. Utilisation of a generalised base platform  
14 is increased by using it during harvesting *and* pollination seasons. Details  
15 of modules developed for use on the vehicle are published separately. The  
16 modules have been built as part of a larger project focusing on automation  
17 in kiwifruit orchards.

18 Automated kiwifruit harvesting and pollination demands computer con-  
19 trol, state-of-the-art manipulators, and machine-vision systems. These sys-  
20 tems are bulky and have specific geometric requirements dictated by the  
21 kiwifruit growing systems. They share the need for electrical power, air pres-  
22 sure, and a means of locomotion. However, they differ in the way they move  
23 when operating. The pollinating module moves at a well-known speed with  
24 minimum changes in angle. This differs from the harvesting module, which  
25 advances a set distance between periods of being stationary. To enable the  
26 whole system to work autonomously, the platform must be able to self-drive  
27 in a way appropriate for both modules.

28 While publishing details of BoniRob, a general purpose robotics platform  
29 for field use, the authors stated that “since the robot development already  
30 includes a high complexity, the application itself should be of comparably low  
31 complexity” (Ruckelshausen et al., 2009). By separating the development  
32 of the platform from other task-specific modules, the risk of a single part  
33 becoming overly complex is reduced.

34 The development of autonomous vehicles in agriculture is not new, but  
35 much of the literature relates to manned vehicles converted to drive-by-wire.  
36 Because the canopy of a pergola-style kiwifruit orchard can droop as low  
37 as 1.4 m to the ground under fruit loading, most standard vehicles are not  
38 suited to this environment. Many autonomous vehicles designed for use in  
39 orchards, such as vineyards, rely on Global Navigation Satellite Systems  
40 (GNSS) for guidance. The dense foliage of a kiwifruit canopy and the sur-  
41 rounding shelter-belts make receiving GNSS signals unreliable at best. The  
42 presented vehicle must navigate through kiwifruit orchards by relying only

- 43 on perception-based sensors. Other requirements for the vehicle are:
- 44 1. support a mass of 1000 kg,  
45 2. fit under a 1.4 m high ceiling,  
46 3. provide 8 kW of electrical power to modules,  
47 4. self-navigate through two test orchard blocks,  
48 5. turn between rows within the headland areas,  
49 6. include a bin-lifting mechanism for carrying fruit bins, and  
50 7. provide a module mounting area no more than 400 mm from the ground.



Figure 1: The presented platform driving through a row of pergola style kiwifruit orchard during winter.

51 **2. Related Work**

52 The introduction of computers and digital camera technology during the  
53 1980s sparked research into autonomous vehicles for agricultural use (Li et al.,  
54 2009). When publishing details of an autonomous vehicle in 1998, Tillett  
55 et al. cite difficulties dealing with variability in lighting and the environ-  
56 ment as the reason no commercial vehicles were available at the time (Tillett

et al., 1998). Their vehicle combined wheel encoders, a compass, and accelerometers for odometry information. It also featured a camera based row guidance system. The system as a whole was capable of spraying individual plants whilst driving autonomously at  $0.7 \text{ m s}^{-1}$  ( $2.5 \text{ km h}^{-1}$ ). While their purpose built experimental vehicle proved capable of row following and targeted spraying, it was not designed for modularity.

Four years later, two autonomous vehicles designed for weed mapping and control in open field crops were presented (Pedersen et al., 2002; Åstrand & Baerveldt, 2002). These platforms had relatively simple chassis and drive systems as they were both at a prototype stage, i.e., neither were designed to carry heavy payloads. The first vehicle, presented by Åstrand & Baerveldt, featured: two-wheel steering, two-wheel drive, a camera based row guidance system, batteries, a combustion engine, and an air compressor. While its appearance was basic, it contained most of the functionality required for use with modularised fruit handling modules. The second unit, described by Pedersen et al., was four-wheel drive with two-wheel steering and used satellite navigation as its primary navigation input. It was battery powered only and lacked any sort of row guidance sensor or power generation unit. The authors found that row-crop based navigation using satellite navigation alone was not practical and proposed the integration of a row-guidance sensor in their next design. They also proposed a revised drive system with four-wheel steering.

Two years later, the revised design proposed by Pedersen et al. (2002) was presented by Bak & Jakobsen (2004). Its drive system was modularised with four identical drive/steering modules mounted to the chassis for locomotion. This revised chassis featured a three-point suspension system that ensured all four wheels stayed in contact with the ground. The system also incorporated the row-guidance sensor as proposed in earlier work, as well as a Real-Time Kinematic enabled GPS receiver (RTK-GPS), fibre optic gyroscope, compass, and wheel encoders. The authors noted that the control strategy for the four independently controlled wheels was non-trivial. While much more developed than the previous work of Pedersen et al. (2002), the platform was not designed to: carry heavy payloads, operate in the absence of satellite navigation, or power itself beyond its battery capacity.

In 2009, details of BoniRob were published by Ruckelshausen et al. (2009). Similar to the previous unit presented by Bak & Jakobsen (2004), it featured a gyroscope, RTK-GPS receiver, and four-wheel steering. It introduced the use of both single-plane and multi-layer laser range scanning, known as lidar,

95 for perception and row detection. A 2.8 kW petrol engine could be mounted  
96 to the chassis, additional to its on-board batteries. It was capable of carrying  
97 a 150 kg payload in its dedicated module space. What made BoniRob par-  
98 ticularly interesting was its ability to alter its track-width by actuating the  
99 legs to which its wheels were mounted. Like the robots before it, BoniRob  
100 was designed for use on open-field crops. During the previous year, some  
101 of these authors published details of a much simpler robot named ‘Weedy’  
102 (Klose et al., 2008), also an open-field crop based sensing platform. BoniRob  
103 represents the first of the more general-purpose platforms designed to carry  
104 modularised payloads.

105 Most recently, Bawden et al. (2017) published details of their field-crop  
106 robot – Agbot II. For locomotion it uses two driven wheels in a differential  
107 drive configuration with castor wheels for support. It is battery powered and  
108 designed to autonomously return to a shipping container with a built-in solar  
109 powered charging station. The vehicle is made of two side modules bridged  
110 by a modular centrepiece containing instrumentation. The side modules  
111 contain the drive system, whereas the centrepiece is designed to be specific  
112 to the application. As with all of the vehicles previously reviewed, its payload  
113 carrying capabilities are limited to ground facing modules, e.g., soil inspection  
114 and weeding.

115 Of particular relevance, is the earlier work of Scarfe et al. on an au-  
116 tonomous kiwifruit picking robot (Scarfe et al., 2009; Scarfe, 2012). That  
117 work involved the creation of a hydraulically driven platform, with two-wheel  
118 steering and four-wheel drive. Four fruit-harvesting arms and a bin-lifting  
119 mechanism were also integrated. While that platform was designed to nav-  
120 igure through kiwifruit orchards autonomously, its ability to do so was not  
121 tested due to an outbreak of *Pseudomonas syringae* pv. *actinidiae* (PSA),  
122 which closed access to kiwifruit orchards. The platform had a petrol en-  
123 gine and made use of camera and lidar based row guidance sensors. It had  
124 sufficient carrying capacity for other roles, however it lacked modularity –  
125 restricting its use to kiwifruit harvesting.

126 With the exception of the platform presented by Scarfe (2012), all of the  
127 reviewed platforms were designed for use with open-field crops. None were  
128 designed for harvesting operations and therefore were not capable of carry-  
129 ing bins. Referring back to the statement from Ruckelshausen et al. (2009)  
130 that “the application itself should be of comparably low complexity”, one  
131 can see why research thus far has focused on simpler tasks such as inspection  
132 or weeding. However, once designs move past these applications it becomes

133 necessary to accommodate other shared requirements. A fork-lift mechanism  
134 is general enough that most orchard related tasks can benefit from it. For  
135 example, during harvesting it can hold a fruit collection bin. During a pol-  
136 lination season it can hold the tank of liquid pollen solution. The ability to  
137 pick up a standard pallet has broad applications in and around orchards too.

138 Reported use of GNSS systems indicate that they are not suitable for  
139 navigating row based crops on their own. With regards to the use of RTK  
140 based GNSS guidance, Slaughter et al. points out the trade-off of requiring an  
141 “unobstructed ‘view’ of the sky from all parts of the field” (Slaughter et al.,  
142 2008). Li et al. (2009) conclude that the use of either GPS and machine  
143 vision, or GPS and lidar will become a development trend. Based on the  
144 increased reception requirements, we discount the use of RTK based systems,  
145 but still consider the use of general purpose GNSS receivers as a navigation  
146 input.

### 147 3. Platform Design

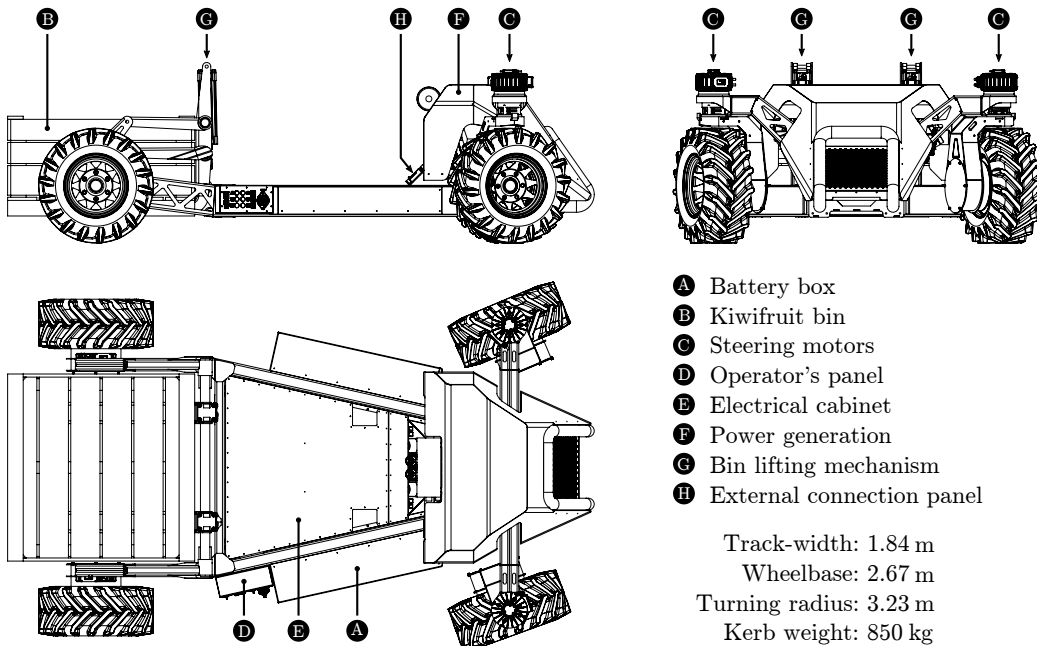


Figure 2: Profile drawings of the robotic platform with kiwifruit bin.

148 The vehicle's design is mostly influenced by the need to carry modularised  
149 robotic systems and fruit bins. Existing commercial platforms suitable for use  
150 in horticulture already exist, such as the Warthog from ClearPath Robotics,  
151 but the maximum payload, battery life, and vehicle geometry make them un-  
152 suitable for kiwifruit harvesting. The mass of robotic modules for pollination  
153 or harvesting can be as much as 600 kg and a bin of kiwifruit adds an addi-  
154 tional 400 kg. The canopy height in typical commercial orchards range from  
155 1.4 m to 1.7 m, so the vehicle must also have a low profile. Modules carried  
156 by the platform require clearance from the canopy in addition to the height  
157 they occupy themselves. To maximise the space available to these modules  
158 the platform must be low-slung at the point they attach. Figure 2 illustrates  
159 the platform's design, with module area allocated between markers 'G' and  
160 'H' in the side-view (top left). The top surface of the chassis in this region  
161 sits 360 mm above the ground.

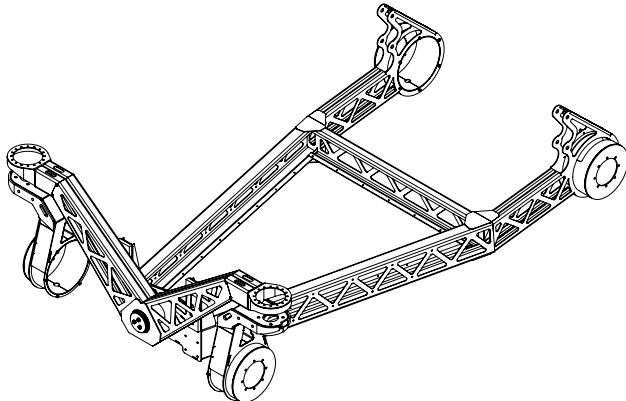


Figure 3: Drawing of the vehicle's chassis showing front pivot mechanism and steering linkages. The laser-cut and folded structure has a total mass of 190 kg.

162 The chassis is assembled from sections of 3 mm laser-cut and folded mild  
163 steel. The sections are welded together on jigs, also made from laser-cut  
164 and folded steel, before being powder coated and assembled. Much of the  
165 folded chassis structure contains triangular cut-outs, reducing weight while  
166 having minimal impact on rigidity. Finite element analysis was used during  
167 the design phase to help identify areas needing to be strengthened and areas  
168 where material could be removed. This helped to ensure the platform meets  
169 its target load capacity of 1000 kg, while the bare chassis weighs only 190 kg.  
170 A drawing of the chassis is shown in Figure 3.

171 Bin lifting forks occupy the area between the rear wheels. Fuel and com-  
172 pressed air tanks sit over the right-hand rear wheel, which can be seen in  
173 Figure 1. The bin lifter is actuated by two vertically mounted double-acting  
174 pneumatic cylinders (SMC CP96D100-320) which are controlled by a pneu-  
175 matic valve block. Each cylinder is capable of exerting 4700 N at 600 kPa or  
176 6300 N at 800 kPa.

177 *3.1. Steering*

178 The steering geometry is Ackermann based, with the front two wheels  
179 being actuated by brushless AC motors (Heinzmann PSM G100). These  
180 motors can generate 7.32 N m of torque with a maximum angular velocity of  
181 3000 rev/min and are rated at 2.3 kW. Their outputs are fed through fixed-  
182 ratio planetary gearboxes with a 64:1 reduction, increasing torque to 470 N m  
183 while reducing the maximum angular velocity to 47 rev/min.

184 Torque requirements for the steering motors are based on a static friction  
185 scenario with the vehicle loaded with a 1000 kg mass, sitting on concrete.  
186 This is described by the following equation:

$$\tau = Wu\sqrt{\frac{B^2}{8} + E^2} \quad (1)$$

187 where  $\tau$  is the torque required to break static friction,  $W$  is the force trans-  
188 mitted through a wheel,  $u$  is the coefficient of friction,  $B$  is the nominal  
189 width of the tyre, and  $E$  is the offset between the tyre's contact surface and  
190 its axis of rotation. The axis of rotation on the vehicle lies directly through  
191 the centre of the tyre, meaning  $E = 0$ . A value of 0.75 was used as the  
192 coefficient of friction as a best guess representation of a tractor-grip tyre on  
193 dry concrete. The mass of the vehicle (800 kg), plus payload (1000 kg), and  
194 fuel (60 kg) adds to 1860 kg. Allowing for uneven weight distribution on the  
195 vehicle and a safety margin, the per wheel mass supported is 500 kg, or a  
196 weight of 4900 N. The width of the tyres is 0.28 m. By combining these  
197 values as per Equation 1, a torque of 388 N is required to overcome static  
198 friction when actuating the steering motors.

199 Actuating the steering wheels independently removes the need for me-  
200 chanical linkages between them, allowing for more extreme steering angles  
201 and a simpler mechanical design. Both steered wheels have the freedom to  
202 rotate 330°, artificially limited by mechanical stops. At the tightest steering  
203 angle of 90°, the centre-point of the turn is located at the midpoint of the

204 rear wheels. The turning radius in this case should be equal to the distance  
205 between the front bumper and the rear wheels (3.18 m).

206 Implementing a four-wheel steering system would shift the pivot point to  
207 the vehicle's centre, roughly halving the turn radius, but this was deemed  
208 unnecessary. Headlands in kiwifruit orchards are sized for tractors with much  
209 larger turning radii than that of the platform. Use of a two-wheeled steer-  
210 ing system removes the need to develop the "non-trivial" control strategies  
211 encountered by Bak & Jakobsen (2004). It also increases the usable area at  
212 the rear of the vehicle by removing the need for clearances around actuated  
213 wheels. A skid steer system was expected to cause ground damage to a level  
214 considered unacceptable to orchard owners when carrying heavy loads.

215 The steering motors have incremental encoders, but no means of absolute  
216 positioning built-in. This means the front wheel angles must aligned before  
217 use. A homing sequence at boot-up is used to find an absolute angle as a  
218 reference for incremental data. Inductive proxy sensors are used as a means  
219 of detecting the position of the wheels during the homing sequence.

### 220 3.2. Drive system

221 The vehicle's three-point suspension system ensures all wheels remain in  
222 contact with the ground. It uses a front pivoting axle to do this, which is  
223 depicted in Figure 3. As the operating speed for the vehicle is  $1.39 \text{ m s}^{-1}$   
224 ( $5.0 \text{ km h}^{-1}$ ), the tyres alone were expected to provide sufficient capacity for  
225 shock absorption.

Performance requirements for the vehicle's traction system during up-hill  
acceleration while under load were calculated as follows:

$$F_{rolling} = C_{rr} \times m \quad (2)$$

$$F_{grade} = m \times G \times \sin(\alpha) \quad (3)$$

$$F_{accel} = m \frac{\Delta v}{t} \quad (4)$$

$$F_{total} = F_{rolling} + F_{grade} + F_{accel} \quad (5)$$

Where  $F_{rolling}$  is the force due to rolling-resistance;  $F_{grade}$  is the grade (or incline) force; and  $F_{accel}$  is the force required for mass acceleration. A rolling-resistance coefficient ( $C_{rr}$ ) of 0.04 was chosen based on values found in an automotive handbook (Robert Bosch GmbH, 2002). It represents the case of a pneumatic tyre on medium-hard soil. Other variables used are: a vehicle mass ( $m$ ) of 1900 kg, slope angle ( $\alpha$ ) of  $20^\circ$ , velocity change ( $\Delta t$ ) of  $2.78 \text{ m s}^{-1}$

( $10 \text{ km h}^{-1}$ ), and an acceleration time ( $t$ ) of 6 s. Putting these values through Equations 2–5 gives a total force requirement of 7.99 kN. On a per wheel basis this is 2.0 kN, or 729 N m when taking the wheel radius ( $r$ ) of 0.365 m into account. Required traction power ( $P$ ) is then calculated as follows:

$$\omega = 2\pi \times \frac{v}{2\pi r} = \frac{v}{r} \quad (6)$$

$$P = \tau\omega \quad (7)$$

where  $\omega$  is the angular velocity of a wheel,  $v$  is the vehicle velocity, and  $\tau$  is torque. At a velocity of  $2.78 \text{ m s}^{-1}$  ( $10 \text{ km h}^{-1}$ ), the calculations give a power requirement of 5.55 kW per wheel.

The selected motors are hub-mounted permanent magnet brushless AC motors with integrated 40:1 fixed-radio planetary gearboxes (Heinzmann PSM-G120). Each motor is rated for 6.4 kW at 96 V with a maximum angular velocity of 3000 rev/min and torque of 20.4 N m. At the output of the gearbox the torque jumps to 816 N m while the angular velocity drops to 75 rev/min; giving the platform a top speed of  $2.86 \text{ m s}^{-1}$  ( $10.3 \text{ km h}^{-1}$ ).

In total there are seven brushless AC motors on-board the platform: four drive motors, two steering motors, and a motor used for electrical power generation. Each are connected to individual AC motor controllers (Sevcon Gen4 DC Size 4). These controllers are available in four bus voltage options: 24-36V, 36-48V, 72V-80V, and 96V-110V. The six motors used for traction and steering are together capable of consuming 30.2 kW. With a 48 VDC bus this would equate to a current draw of 630 A. As 24 m of cabling is required to connect the motors and controllers to a common point on the vehicle, a 96 VDC bus was used to reduce the required gauge of that cable.

### 3.3. Power Distribution

The system bus connects the batteries and generator to motor controllers and on-board power converters. A series of heavy-duty contactors (TE Connectivity Kilovac LEV200) control each device's connection to the bus, as well as the bus's connection to the power source. Figure 4 illustrates the distribution of power on the platform.

Two battery modules attached to the sides of the chassis each house fifteen lithium-iron-phosphate ( $\text{LiFePO}_4$ ) batteries connected in series. Together, the batteries (Winston/Thundersky WB-LYP90AHA) provide a nominal bus voltage of 96 V and a total electrical capacity of 8.64 kWh. The battery packs were manually ‘bottom-balanced’ before being fitted and no cell-level

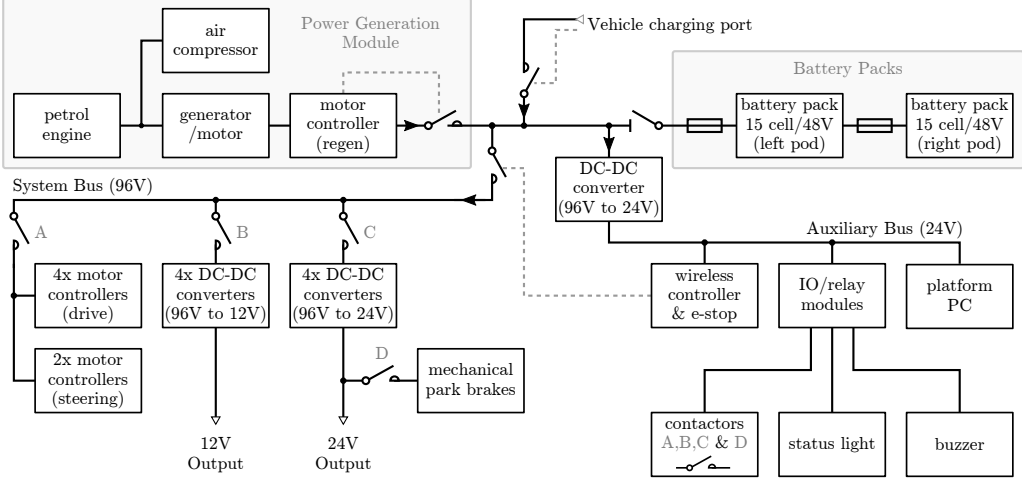


Figure 4: Power distribution system diagram. Dashed lines in grey indicate control lines to contactors.

voltage monitoring is present. Maximum and minimum pack voltages were established by monitoring individual cells during charging and discharging. At the point that any individual cell exceeds a safe maximum/minimum threshold, the respective maximum/minimum pack voltage is determined.

A hermetically sealed disconnect switch (Gigavac HBD41) isolates the batteries from the system. Once closed, an auxiliary 24 V bus becomes active that powers components required to bring the rest of the rest on-line.

A power generation unit comprised of a petrol engine (Honda GX-690), air compressor (Rotorcomp NK-1), and electrical generator is housed at the front of the vehicle. The drive shafts of these units are connected via pulleys and a heavy-duty timing belt. The engine, compressor, and alternator are controlled and monitored by a micro-controller based control board. This board connects to the Platform PC via the system CAN bus. The engine is capable of producing 16 kW, where up to 9.6 kW is converted to electrical power, limited in software, and 4.0 kW is converted to pneumatic power. The system maintains a pneumatic tank pressure of 600 kPa to 800 kPa.

Electrical generation is done with a brushless AC motor/generator (Heinzmann PMSG-150) connected to the same model of motor controller used with the drive system. This motor was a larger variant of those used for traction and steering, minus the gearbox. Its controller was configured only to have regenerative braking functionality, i.e., power could not be applied

276 to the motor. This configuration allowed the system to control the rate of  
 277 power generation by commanding braking effort from the controller. The  
 278 controllers provide battery voltage and current limits as well as the ability  
 279 to reduce effort as the battery becomes fully charged. These settings provide  
 280 all the functionality of a general purpose battery charger, making this a cost  
 281 effective and versatile charging solution. Electrical energy from the power  
 282 generation unit is fed to the batteries in a series-hybrid configuration. An  
 283 external charging port is also fitted to allow charging of the batteries directly.

284 A fuel tank is fitted over the rear right-hand wheel, visible in Figure 1.  
 285 It can hold 60l of petrol, allowing the vehicle to operate continuously for  
 286 over 24 h. On-board DC-DC converters deliver 2.8 kW at 12 VDC, 3.8 kW at  
 287 24 VDC, and 3.5 kW at 240 VAC, simultaneously. A connection panel at the  
 288 front of the dedicated module area houses the weather-sealed plugs through  
 289 which these outputs are accessible.

### 290 3.4. Communications Architecture

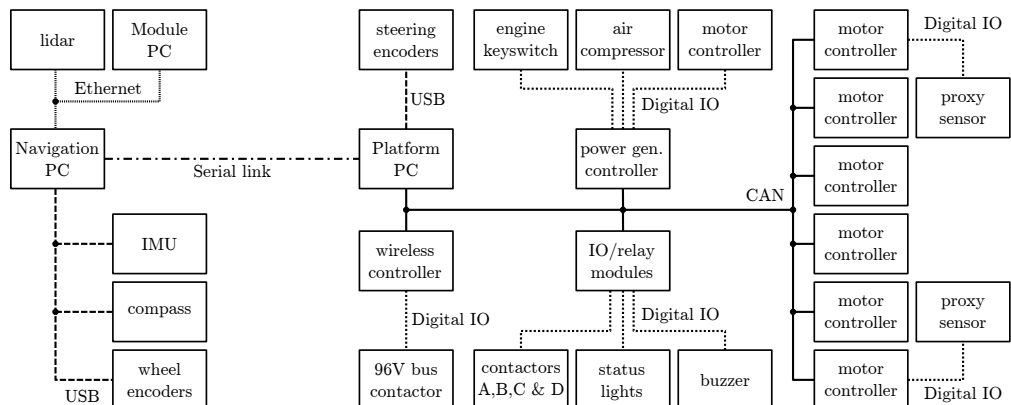


Figure 5: Communications level system diagram showing types of links between devices. Devices on right-hand side of the serial link are mechanically integrated into the vehicle, whereas those on the left are modular and can be removed.

291 The platform is centrally controlled by an x86 based small-form-factor  
 292 PC (Intel NUC) running Ubuntu 16.04 server edition, referred to as the  
 293 “Platform PC”. This computer communicates with most sub-systems via a  
 294 CAN bus interfaced using a USB adaptor (IXXAT USB-to-CANV2).

295 A second, externally mounted, computer is responsible for higher level  
 296 control of the vehicle. It is used to connect to navigation sensors, send drive

297 commands to the platform, and perform processing tasks relevant to au-  
298 tonomous navigation. It too is an x86 based PC running Ubuntu, but uses  
299 a commodity microATX form-factor motherboard with a discrete graphics  
300 card (Nvidia GTX 1080Ti). The graphics card is used to accelerate neural  
301 network algorithms and some image processing functions. An Ethernet net-  
302 work connects this PC to the mounted payload modules, while a RS422 serial  
303 link is used to communicate with the Platform PC. Figure 5 illustrates this  
304 arrangement.

305 In addition to the drive commands generated by the Navigation PC, a  
306 wireless controller (HBC Radiomatic Eco) lets the operator issue drive com-  
307 mands via joystick. The receiver module contains relays that are directly  
308 controllable from the remote control. All inputs from this controller are also  
309 broadcast on the CAN bus and read by software nodes on the Platform PC.  
310 The remote control has two joystick inputs, two selector switches, four but-  
311 tons, and an emergency stop switch. The emergency stop switch is connected  
312 to the 96 V bus contactor via relay outputs from the receiver unit. If this  
313 switch is closed during operation, or the controller goes out of range, power  
314 to the bus is cut within 500 ms. This engages the mechanical park brakes, re-  
315 moves all tractive effort from the motor controllers, and de-powers mounted  
316 modules.

317 The open source Robotic Operating System (ROS) is used to facilitate  
318 communication between computers and software nodes running within each  
319 computer. Nodes written using this framework follow either a publish-  
320 subscribe or service-client pattern. To maximise code reusability, each device  
321 on the platform has its own ROS-compatible node dedicated to publishing de-  
322 vice data or subscribing to generated device commands. Interface adapters,  
323 motor controllers, wireless controllers, lidar, and encoders are examples of  
324 devices with dedicated interface nodes. Nodes are also used to transform  
325 or perform calculations on data while passing it between nodes written in  
326 either C++ or Python. For instance, as shown in Figure 6, an ‘Ackermann  
327 kinematics’ node transforms steering input data into individual wheel veloc-  
328 ity and position/angle outputs. Among other things, ROS offers the ability  
329 to monitor and record all communication passing through it which can be  
330 replayed and interrogated at a later date.

331 The manufacturer’s configuration of the motor controllers require them  
332 to be interfaced using a combination of analogue and digital inputs. For  
333 example, the accelerator and steering inputs are controlled by potentiometers  
334 actuated by the vehicle’s driver. However, the controllers also provide an

335 option for a multi-motor vehicle configuration. In this configuration, the  
336 analogue inputs fed into a master controller are relayed to a second controller  
337 over a CAN interface. This interface is configured using a proprietary tool  
338 and is not intended for use other than between controllers configured with  
339 their software. By observing the communication protocol between a master  
340 and slave in operation, it was possible to implement a master node in software  
341 that runs on the Platform PC. With this, all motor controllers on the platform  
342 are programmed as slave devices. This allows them to accept drive commands  
343 via CAN interface, allowing them to be directly controlled by ROS nodes.

344 Relay modules allow the Platform PC to toggle power to on-board power  
345 supplies, motor controllers, park-brakes, and lights. They also monitor the  
346 timing of synchronisation messages transmitted by the Platform PC onto  
347 the CAN bus. These synchronisation messages are configured to occur every  
348 20 ms as an indication that the system is running as expected. Once a relay  
349 module detects an absence of these messages for 100 ms or longer it enters an  
350 error state. This causes the motor controllers and on-board power supplies  
351 to be shut-off and the park-brakes to be engaged. Synchronisation message  
352 monitoring is used as a fail-safe mechanism to ensure the system is promptly  
353 shut-down if the Platform PC fails.

354 The open source simulation package Gazebo was used to simulate the  
355 vehicle's steering geometry with input from a game-pad. This revealed is-  
356 sues that were resolved before implementation on the physical hardware. It  
357 also provided the opportunity to tune control parameters, such as steering  
358 sensitivity, while reducing the time to test.

#### 359 4. Navigation Sensor Selection

360 The choice of sensors incorporated into a vehicle determines which algo-  
361 rithmic approaches are available for navigation and object detection. Lidar,  
362 cameras, and GNSS receivers have been considered. Each sensor's ability to  
363 capture relevant data is evaluated by in-orchard trials.

364 Other sensors considered for inclusion are outlined in Table 1 along with  
365 their associated issues. Factors considered were the strengths and weaknesses  
366 in the context of orchard use, reported usage in literature, and availability at  
367 a suitable price. A review of previous works highlighted both lidar and 2D  
368 cameras as offering high functionality for navigation and object detection.  
369 Time-of-flight cameras are a compelling option based on a cost-benefit anal-  
370 ysis; especially if cheaper units work outdoors in the presence of sunlight.

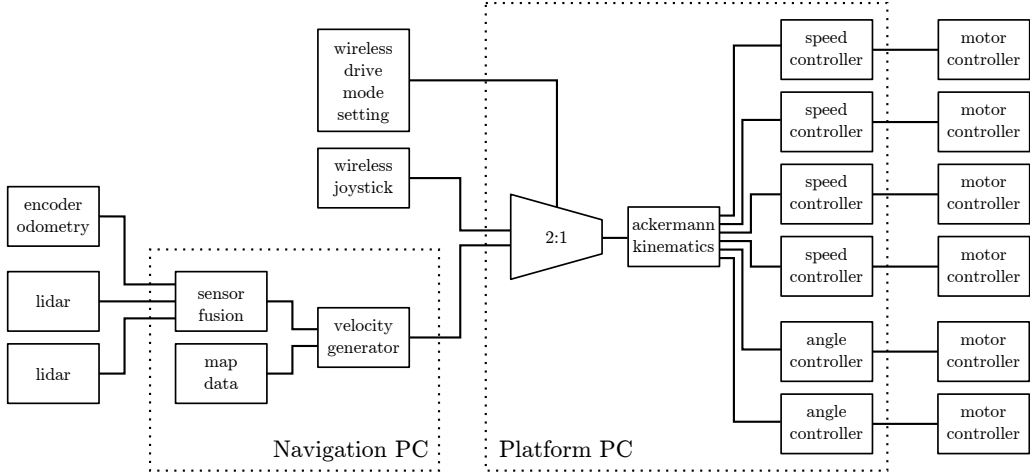


Figure 6: Simplified diagram showing connectivity between ROS nodes used for manual and autonomous platform control.

371 Because localisation is such a key function, the performance of two GNSS  
 372 receivers has also been evaluated.

Sensor Type	Common Issues
GNSS receiver	Prone to signal loss from surrounding foliage
Inertial Measurement Unit	Error accumulation and thermal drift
Digital Compass	Prone to disturbance by nearby metallic structures
Encoder	Error accumulation
Lidar	Reduced visibility in fog and heavy rain
Time of Flight Camera	Reduced visibility in sunlight, fog and heavy rain
Camera	Reduced visibility in fog or direct sunlight
Thermal Camera	Reduced visibility in conditions of low thermal contrast

Table 1: Sensor types considered for inclusion on the platform.

373 As the drive motors have built-in wheel encoders, basic odometry data is  
 374 already available. Encoders on driven wheels will give false readings if wheel  
 375 slippage occurs so are not be used for odometry alone. However, the data  
 376 provided can still be used to assist with mapping, localisation, and provide  
 377 velocity feedback.

#### 378 4.0.1. In-orchard Camera Evaluation

379 Three types of camera were tested: time-of-flight, 3D stereoscopic, and  
 380 traditional 2D cameras. Smaller platforms (Clearpath Husky and Adept

381 MobileRobots Pioneer P3-AT) were used to gather data used for evaluation.  
382 Cameras were mounted 0.8 m above the ground, roughly mid-way between  
383 the ground and the canopy, facing forward.

384 The time-of-flight camera was a Basler TOF640-20GM-850NM. It pro-  
385 vides range, intensity, and confidence data at a resolution of 640 by 480  
386 pixels. This specific model was chosen as it had previously proved useful  
387 when collecting depth data of kiwifruit canopies. During that time it had  
388 been operated under a range of lighting conditions and exhibited minimal  
389 occurrences of data loss. In those conditions the camera was mounted with  
390 its principal axis aligned vertically, pointing upwards to the canopy. How-  
391 ever, subsequent testing with the camera mounted with its principal axis  
392 aligned horizontally revealed significant data loss in both sunny and overcast  
393 conditions. This is thought to be the result of two factors. The first is a  
394 lower reflectivity of objects in view of the camera when facing forwards, as  
395 opposed to facing up at a leafy canopy. The second is due to a dramatic  
396 increase in distance between the camera and the scene's subject matter. As  
397 the camera relies on active illumination of the scene, its ability to detect that  
398 illumination amongst ambient light will drop sharply with distance.

399 The 3D stereo camera tested was an Intel RealSense R200. It combines  
400 a stereo pair of infra-red cameras with a colour camera. Additionally, it  
401 features an infra-red projector as a means of adding texture to objects in its  
402 field of view to assist with stereo processing. The appealing characteristics  
403 of this sensor were its low cost and its claim of being long-range and able to  
404 work outdoors. However, in both overcast and sunny conditions it suffered  
405 from a *complete* loss of range data. This appeared to be the result of ambient  
406 light interfering with the infrared projector's signal.

407 Traditional, 2-dimensional, cameras trialled were the Basler Dart daA1600-  
408 60uc, Flir CM3-U3-13S2C-CS, and a Logitech C920 web-camera. The Logi-  
409 tech C920 suffered from significant motion blur that, being a consumer grade  
410 web-camera, was not surprising. It also lacked the functionality of a hard-  
411 ware trigger and sent images with significant latency, measured at 150 ms.  
412 The Basler and Flir cameras both produced images of sufficient quality and  
413 featured hardware triggering. The Basler camera had a USB3 interface and  
414 an average image transfer time of 14 ms. The Flir camera had a USB2 in-  
415 terface and an average image transfer time of 65 ms. The Basler offering  
416 was favoured for its later model image sensor, simpler software interface, and  
417 lower-latency.

418 Both the time-of-flight and 3D stereoscopic camera systems were deemed



Figure 7: Example images captured from trialled 2D cameras. Basler Dart daA1600-60uc (left), Flir CM3-U3-13S2C-CS (centre), Logitech C920 web-camera (right).

unsuitable based on the occurrences of data loss. Images from the industrial 2D cameras (from Basler and Flir) were deemed suitable for object detection and classification. This was verified by processing the data using readily accessible detection algorithms such as convolutional neural networks. Using a pair of these 2D cameras it is also possible to build a stereoscopic pair. This provides the same functionality of the 3D stereoscopic camera from Intel, but without requiring the infra-red projector. Stereo pairs of industrial cameras have since proven useful on modularised harvesting and pollination modules for localising fruit and flowers, but were not tested for row following.

#### 4.0.2. In-orchard Lidar Evaluation

Three lidar were evaluated, two single-plane and one multi-layer. The two single-plane lidar were the Hokuyo UTM-30LX and a SICK LMS111. The multi-layer lidar is a Velodyne VLP-16 which has 16 horizontal 360° planes spread over 15° vertically. Data was collected from each lidar by driving through orchard rows with the sensor placed 0.8 m above ground level. Data was captured both on the presented platform and the smaller robots used to collect camera data.

The intention was to use lidar as a means of detecting structure defining features of the orchard, such as posts, trunks and hedges. Detecting these features should allow for row boundary detection and general mapping and localisation. However, both single-plane lidar produced clouds of unstructured data amongst the structured features, as shown in Figure 8. This was caused by the lidar scan plane intercepting with the canopy whilst driving over convex terrain. Similarly this issue arose on concave terrain where the plane intercepted with the ground. This situation is depicted in Figure 9.

The issue was reduced by the use of a multi-layer lidar and post-processing.

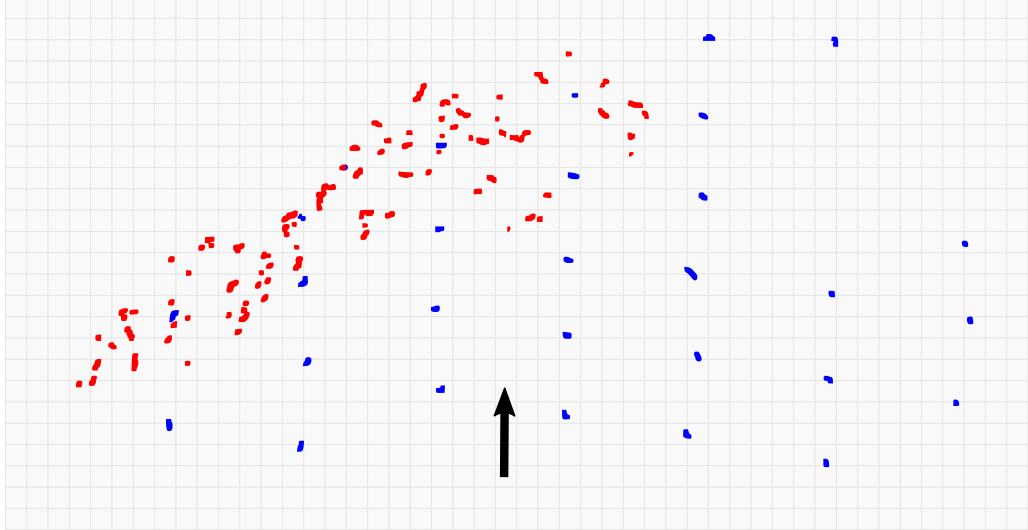


Figure 8: Data captured from a single plane lidar showing non-structural points reflected by the canopy (indicated by red markers) and structural points from tree trunks and posts (blue markers). The arrow indicates the position and heading of the platform at the time of capture.

Having sixteen layers available meant it was possible to select a scan layer that gives the most useful viewing range. Referring again to Figure 9, that would correspond to the dotted line above the horizontal (dashed) line which intercepts with a row defining feature (a tree trunk).

It was decided that a multi-layer lidar would be best suited for navigation due to its ability to see more distant features while driving on undulating ground. A single-plane lidar could still be used at short range as an independent channel of processing for redundancy or obstacle detection.

#### 4.0.3. In-orchard GNSS Evaluation

Two GNSS receivers were evaluated: a Ublox Neo-M8N module and an OmniSTAR 5120VBS with AX0 series antenna. Both were connected to a single board computer (Beaglebone Black). The Ublox module was selected for its high sensitivity and internal low-noise amplifier. It was capable of receiving GPS, Galileo, GLONASS, and BeiDou GNSS signals concurrently. The OmniSTAR receiver was chosen for its external high-gain antenna (34 dB) which claims multi-path rejection. It was capable of receiving only GPS signals.

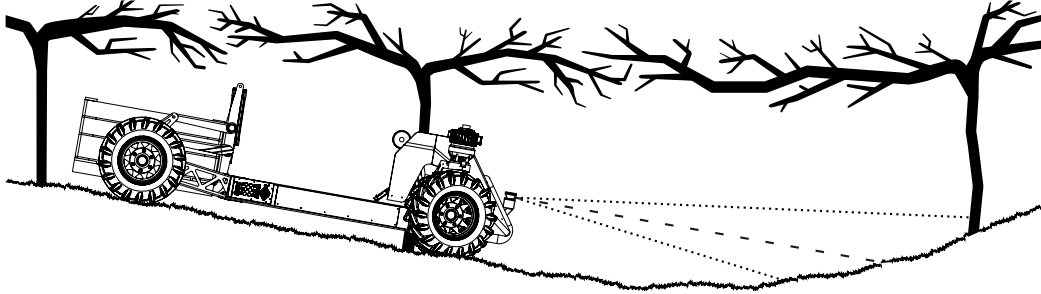


Figure 9: On concave slopes the lidar scan plane can intercept with the ground before striking row features. The dashed line shows a horizontal plane coming from the the lidar. Dotted lines represent the upper and lower layers taken from the multi-layer lidar.

462 The testing procedure first involved planning a path through a single row  
 463 of a kiwifruit orchard and plotting this on a satellite map. The receivers  
 464 were then tested separately over the course of approximately two hours by  
 465 walking them along the planned path. Before testing, each unit was powered  
 466 up and given 30 min to initialise in an open area near the kiwifruit orchard.  
 467 During testing, each unit was walked slowly along the predetermined path  
 468 with stops at each waypoint to provide time for a positional fix. The path was  
 469 approximately 500 m in length and took approximately 15 min to complete,  
 470 including stops at each waypoint. Way-points were spaced at intervals of  
 471 5.5 m along the row.

472 The path followed, together with coordinates collected from the receivers,  
 473 are presented in Figure 10. It should be noted that data has been recorded for  
 474 the round-trip so represents two passes along the path. It was noticed during  
 475 testing that the signal quality lights on both receivers regularly indicated a  
 476 loss of signal.

477 The Omnistar unit appears to track the approximate path well, but the  
 478 data is sparse with regular loss of signal after entering the orchard. The  
 479 Ublox unit collected more data, but was much less accurate. It may be pos-  
 480 sible to use a unit such as the Omnistar, which provided fewer but more  
 481 accurate readings, as a sanity check for an approximate location within or-  
 482 chards. Overall, the units could not be relied on for localisation in this en-  
 483 vironment. These results indicate GNSS receivers with similar performance  
 484 to those trialled are unsuitable for use in kiwifruit orchards.

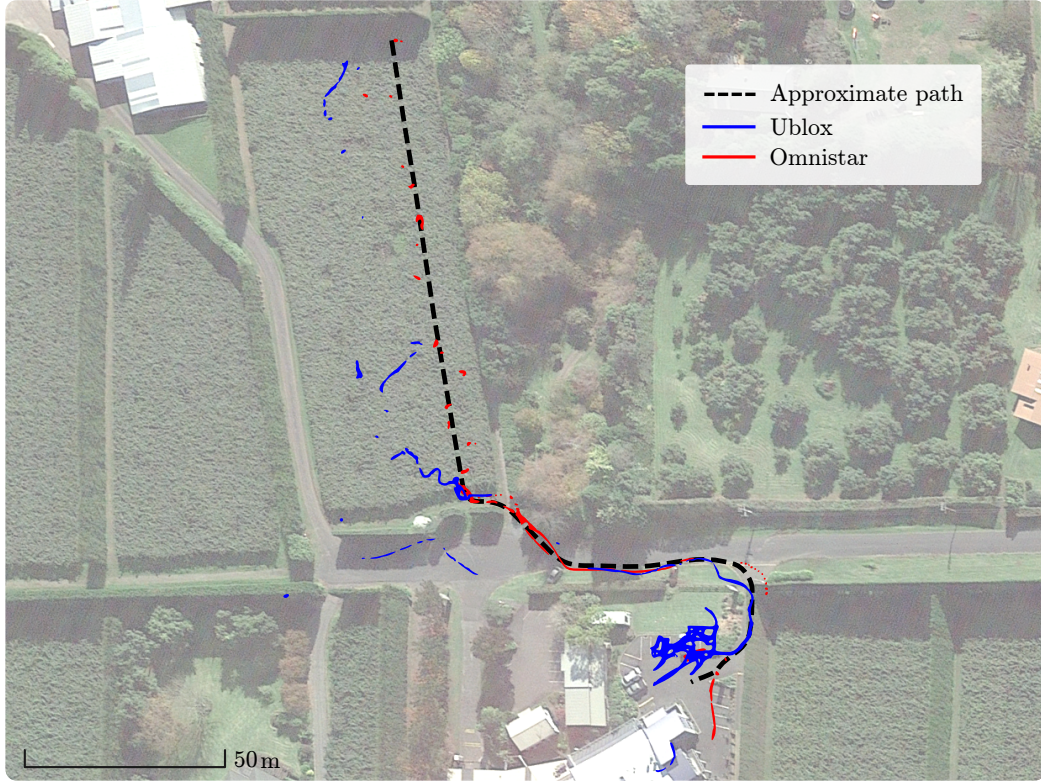


Figure 10: Aerial view of the path taken through the test orchard and the captured GPS data. Dashes representing the approximate path are spaced at intervals of 5.5 m.

## 485 5. Autonomous Block Traversal

486 Two row following strategies were developed for implementation on the  
 487 platform. Further details and results of each have been published separately.  
 488 One method used multi-layer lidar to detect the trunks and posts of the  
 489 orchard and follow a centre-line between them (Bell et al., 2016). The second  
 490 method used a single camera combined with a convolutional neural network  
 491 to segment features within the image. These features were: traversable space,  
 492 tree-lines, and row-ends (Bell et al., 2017). A centreline was then fitted to  
 493 the areas marked as traversable and used to generate a control vector.

494 Both algorithms were developed on smaller, commercially available, test  
 495 platforms while the target platform was under construction. A laptop (Dell  
 496 E6410) with integrated graphics processor (Nvidia M5000M) was used on  
 497 those platforms to process sensor data and generate drive vectors. Both

498 approaches produced paths that led to reproducible row following behaviour.  
 499 A method of conducting row-end turns was trialled on the Pioneer 3-AT robot  
 500 using the lidar based approach. However, the platform's drive system lacked  
 501 the power required to turn into rows on uphill slopes.

502 To determine when the vehicle was at the end of a row, the multi-layer  
 503 lidar was used to detect the absence of canopy in a volume above the front  
 504 and to the sides of the vehicle. The camera based method was unable to  
 505 detect this end-of-row condition which is necessary for initiating the turn. It  
 506 also lacked the ability to locate obstacles which is important on the target  
 507 platform due to its size and power. Finally, the lidar based approach required  
 508 much less computational power to achieve similar performance. While it  
 509 would be possible to combine the approaches, only the lidar based method  
 510 was adapted for use on the target platform.

511 Differences in the geometry meant adjustments were needed when imple-  
 512 menting on the target platform. The multi-layer lidar was mounted hori-  
 513 zontally above the front-right steering motor, visible in Figure 1 and later  
 514 in Figure 12. The smaller platforms used a skid-steer geometry, whereas  
 515 the target platform uses an Ackermann geometry. This means that when  
 516 turning, a skid-steered platform pivots along a lateral axis passing midway  
 517 between the front and rear wheels. On the target platform, that axis instead  
 518 passes through the rear axle. The software was modified to account for the  
 519 change in pivot axis and mounting location of the lidar.

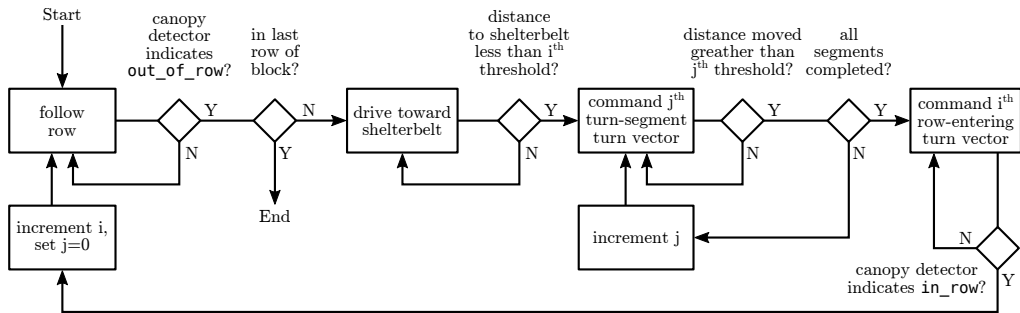


Figure 11: Flow-chart of the developed autonomous block traversal algorithm.

520 Figure 11 depicts the steps taken when traversing a block, including exe-  
 521 cution of the row-end turns. The multi-layer lidar is used to detect whether  
 522 the vehicle is *in\_row* or *out\_of\_row* based on the presence of canopy. A row-  
 523 end turn sees the platform execute a series of turn-segments which have

524 previously been tuned for the specific row and direction of turn. Initially,  
525 a template set of turn-segments is executed at each row's end while under  
526 observation. If the vehicle gets too close to obstacles or nearby boundaries  
527 during execution, the operator would intervene before collision occurs.

528 A row end turn can contain any number of segments, with each repre-  
529 senting a turn vector and distance that must be covered before proceeding.  
530 Once the operator intervenes, he/she will tweak relevant parameters of the  
531 turn. This can be widening or tightening as well as lengthening or short-  
532 ening the distance of the segment. Finally, if an object is detected in the  
533 vehicle's path during a turn, the steering is automatically adjusted to avoid  
534 the object. This happens independently from the parameters contained in  
535 the map file. Figure 12 shows the platform performing a row-end turn while  
536 under autonomous control.



Figure 12: A row end turn being performed autonomously by the platform. The multi-layer lidar (Velodyne VLP-16) is visible above the front-right steering motor.

537 **6. Testing**

538 *6.1. Mass Loading*

539 Structural integrity testing was carried out by loading a 1100 kg mass to  
540 the vehicle's module area. No deflection of the vehicle's chassis structure  
541 was evident upon application of the test mass. Deflection of 1.5 mm was  
542 measured between the front pivot and the wheel supports. Static steering  
543 tests conducted on a dry concrete surface showed no reduction in ability to  
544 turn while supporting the test mass. Dynamic tests involved three instances  
545 of stopping at a 10° descent at a speed of 10 km h<sup>-1</sup>. During each test the  
546 vehicle came to a complete stop within 2.0 m.

547 *6.2. Drive System*

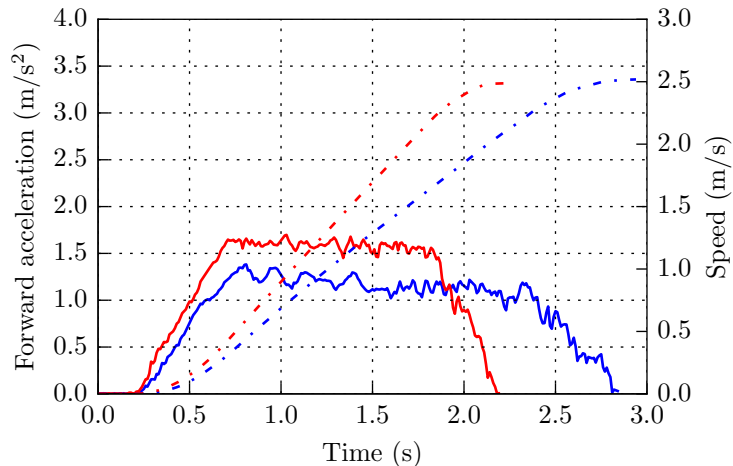


Figure 13: Acceleration of the platform on level ground (red) and up a 3.5° incline (blue).

548 Drive system testing had the platform accelerated from a stand-still un-  
549 der manual control to its maximum speed on both level ground and up a  
550 3.5° incline. The acceleration was measured using an Inertial Measurement  
551 Unit (IMU, LPMS-USBAL2). Figure 13 shows the acceleration profile of  
552 the platform during both tests. The platform's weight during the test was  
553 estimated to have been  $(850 \pm 50)$  kg in each case.

554 In both instances the vehicle reached a top speed of  $2.5 \text{ m s}^{-1}$  ( $9.0 \text{ km h}^{-1}$ ),  
555  $0.28 \text{ m s}^{-1}$  short of the target speed. During the acceleration test on level

556 ground, a peak power of between 684 W to 770 W, and torque of between  
557 930 N m to 1046 N m was calculated per wheel. During the inclined acceler-  
558 ation test, a peak power of between 542 W to 610 W, and torque of between  
559 779 N m to 876 N m was calculated per wheel. The torque calculations sug-  
560 gest the motors are developing their specified output of 816 N m. The mo-  
561 tor controllers are configured to supply extra torque for short bursts, which  
562 could explain why the calculated torque on level-ground is higher than this  
563 value. The inclined test began with the vehicle being held stationary using  
564 torque-control, which may have affected the controller's ability to produce  
565 the higher peak torque in this case. The lower than expected top speed in  
566 both cases suggest there are configuration issues with the motor controller's  
567 speed setting.

### 568 6.3. Turning Circle

569 Measurements of the vehicle's turning radius were performed at speeds  
570 of  $1.39 \text{ m s}^{-1}$  ( $5.0 \text{ km h}^{-1}$ ) and  $2.78 \text{ m s}^{-1}$  ( $10.0 \text{ km h}^{-1}$ ) on both dry tarmac  
571 and damp grassland. These speeds were calculated at the mid-point between  
572 the two front wheels. Having a wheelbase of 2.67 m, these speeds equate to  
573 angular velocities of  $0.520 \text{ rad s}^{-1}$  and  $1.04 \text{ rad s}^{-1}$  respectively.

574 In each test, a line was drawn on the ground in front of the vehicle to  
575 mark its starting position. The vehicle was then turned through an angle  
576 of  $(180 \pm 10)^\circ$  under manual control with the steering angle set at  $90^\circ$ . The  
577 final angle was adjusted using odometry information to ensure the total angle  
578 was within  $(180 \pm 3)^\circ$ . A marker was then drawn on the ground at the  
579 front of the vehicle at this position. The distance between the markers was  
580 measured at 6.45 m for both surface types and both test speeds. This gives a  
581 turning radius of 3.23 m, 0.05 m wider than the estimate based on kinematic  
582 calculations. The authors put this discrepancy down to the quality of the  
583 angular calibration of the front wheels.

### 584 6.4. Bin Lifter

585 A pallet mounted mass of 370 kg was used to test the bin lifter. The  
586 lifter's pneumatic valve block was manually activated until the pallet sat  
587 250 mm above the ground. To raise the load, pneumatic pressure of 800 kPa  
588 was applied to one port of each double acting cylinder while the other port  
589 was opened to atmosphere. Lowering was done by simply opening both ports  
590 to atmosphere and allowing the load to descend under its own weight. The

591 load was lifted and lowered a total of five times. The vehicle was driven for  
592 300 m with the load, which included an 3.5° incline for 30 m.

593 The lifting capacity of the mechanism was sufficient to raise the load gently  
594 to its target height. At its lower position, signs of imbalance between the  
595 two cylinders was evident, which caused shuddering. The shuddering was  
596 due to excessive and unbalanced static-friction on each side of the four-bar  
597 mechanism. This friction was caused by overly tight-fitting sleeve bearings.  
598 The behaviour was also evident when hand actuating the lifter. Whilst driving,  
599 the load dropped by between 60 mm to 70 mm from its initial height.  
600 This drop, and the variation in resting position, was thought to be caused  
601 by the combination of static friction and driving related vibrations.

## 602 *6.5. Turning Between Rows*

603 Two orchards were used for row-turn testing, where a single block was  
604 used at each. These blocks are referred to as Block A and Block B. Block A  
605 was 1.15 km in total traversable length spread over 10 rows, while Block B  
606 was 670 m in total traversable length spread over 9 rows. After tuning of the  
607 row end turning manoeuvres, the platform navigated Block A consecutively  
608 7 times. Figure 14 shows the number of interventions per traversal while  
609 under tuning in Block A, 19 traversals in total. After tuning the row end  
610 turns in Block B, it was navigated 3 times consecutively. Figure 15 shows  
611 the number of interventions per traversal while under tuning in Block B, 10  
612 traversals in total.

613 The key weakness of the current navigation system is the need to tune  
614 the row end turns manually for each site. The tuning required for the first  
615 orchard block amounted to eight traversals of the entire block. For the second  
616 block, seven complete traversals were required for tuning. This creates a  
617 significant resource overhead for deployment to any new sites. If the row  
618 end turns are not sufficiently tuned, two failure cases may occur. The most  
619 common case is that the vehicle turns through a row end too tightly or not  
620 tightly enough and the object avoidance system is not sufficiently responsive  
621 to avoid a collision. All but four interventions were due to an imminent  
622 collision with a post during a row end turn. Three interventions during row  
623 end turning were due to the platform trying to recommence row following  
624 before facing the new target row. In this case the most feasible path for row  
625 following was detected through the headland area, instead of the target row.  
626 One intervention, attempt 12 of Block A, was caused by the canopy detection  
627 system triggering a row-end turn whilst still inside a row.

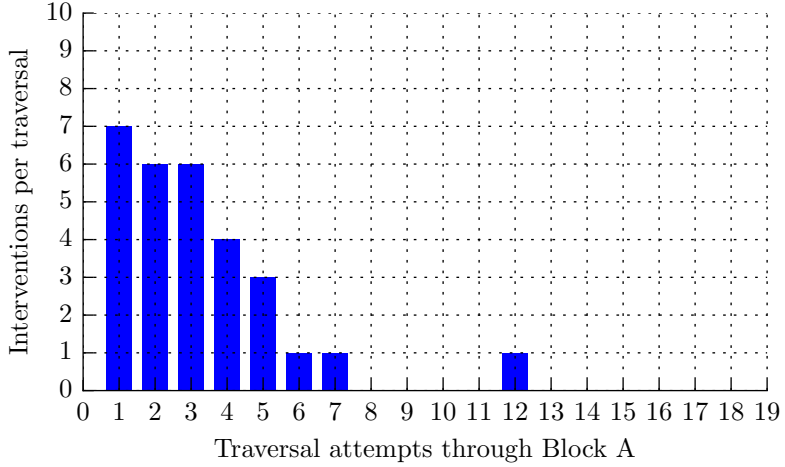


Figure 14: Number of interventions during tuning of row-end turns throughout Block A.

### 628 6.6. Row Following

629 Row following repeatability tests were made by allowing the platform  
 630 to self-drive through a row, from the same starting point, five times. The  
 631 algorithm used was similar to that reported in Bell et al. (2016), but had  
 632 a couple of alterations. It used only a multi-layer lidar (Velodyne VLP-16)  
 633 and an IMU (LPMS-USBAL2), but made no attempt to avoid obstacles. Its  
 634 end-of-row detector was based on the vehicle’s proximity to the row’s last  
 635 pair of posts, as opposed to detecting the absence of canopy above.

636 Each test was conducted at the vehicle’s target operating speed of  $1.39 \text{ m s}^{-1}$   
 637 ( $5 \text{ km h}^{-1}$ ). To determine the vehicle’s trajectory, recordings of the lidar and  
 638 IMU were made and run through a SLAM package off-line. The SLAM  
 639 package used was Cartographer (version 1.0) used as a ROS package that  
 640 produced both the map and the vehicle’s trajectory information (Hess et al.,  
 641 2016). The spacial resolution of the SLAM map was 0.05 m/pixel. Wheel  
 642 odometry provided by the drive motors was not used during row following  
 643 as signs of slippage were apparent. Quick measurements conducted on grass  
 644 showed an imbalance of approximately 5 % between the rear wheels depend-  
 645 ing on ground slope.

646 Figure 16 shows the resulting orchard map and five trajectories overlaid  
 647 on top of each other. While differences in start position are estimated to  
 648 be less than 0.1 m, the trajectories show a spread of 1.69 m. The total path

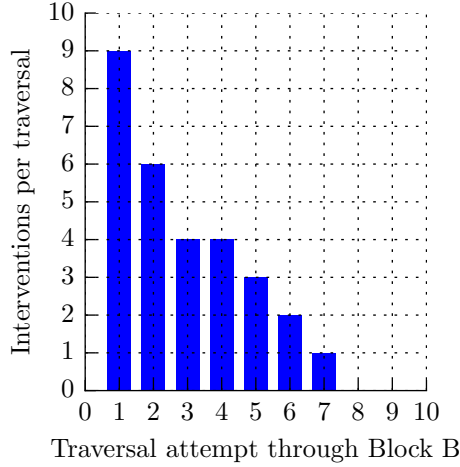


Figure 15: Number of interventions during tuning of row-end turns throughout Block B.

Test number	Path length
1	106.66 m
2	103.70 m
3	104.13 m
4	104.47 m
5	104.37 m

Table 2: Total path length for each row-following test. The average length is 104.67 m and the range is 2.96 m (2.82 %).

length for each run is listed in Table 2. Figure 17 shows an analysis of the path following performance. This involved measuring the midpoints between each post/trunk pair manually using vector drawing software and comparing these midpoints to each path. Sources of error were  $\pm 1$  pixel at either end of the midpoint measurement lines as well as rounding errors. Figure 19 quantifies the divergence of each path from the average location recorded between each trunk/post pair. Figure 20 shows the end-points for each run relative to the row features at the end of the row.

Analysis of the tracking performance is particularly difficult as the positioning of the posts/trunks show obvious signs of deviation, evident in Figure 18. For example, the dip at post/trunk pair twenty-two in Figure 17 corresponds with the post/trunk pair near the 58 m mark in Figure 18. Similarly, the peak at position 26 corresponds to the post/trunk pair near the

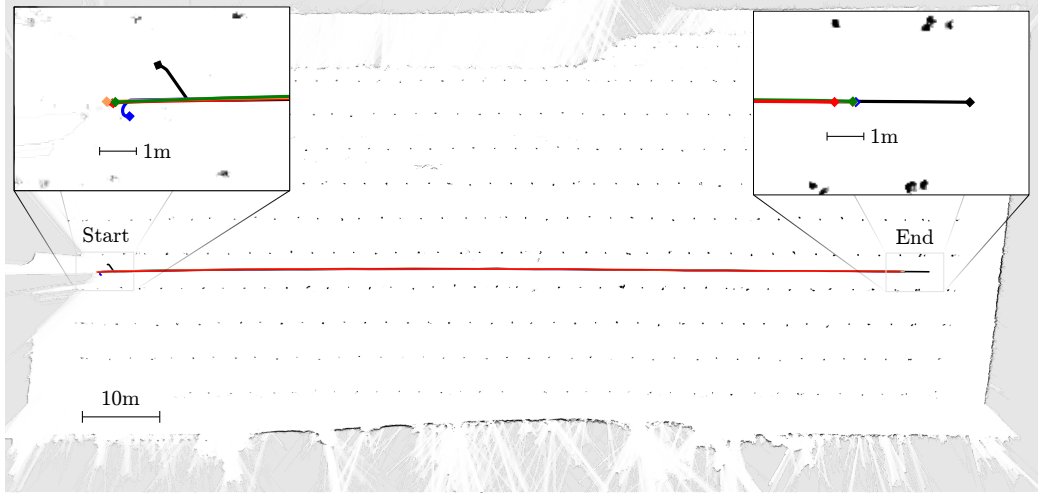


Figure 16: Five paths taken during a sequence of row-following repeatability tests.

662 70 m mark. Without significant corrections to the data, which would be sub-  
 663 jective, the analysis describes more about the linearity of the orchard’s row  
 664 defining features than the path tracking performance. It is apparent how-  
 665 ever from Figure 18 that the vehicle’s path is relatively straight and remains  
 666 unperturbed by the non-linearity in positioning of the row’s features.

667 Figure 19 quantifies the deviation between each trial relative to the mean  
 668 path taken over the five trials. It shows that the worst case repeatability was  
 669 less than  $\pm 75$  mm.

670 Finally, Figure 20 shows the end position of each path. The path-following  
 671 algorithm determines the end position based on its proximity to the last post-  
 672 pair within its detection range. Notice that the last post in each row is spaced  
 673 slightly further than is usual inside the row. This is visible along the left hand  
 674 side of the SLAM map shown in Figure 16 and in the photo of Figure 12.  
 675 That extra spacing places the final post-pair near the software-defined cut-off  
 676 region used to identify post/trunk pairs. Stopping slightly earlier results in  
 677 the last post/trunk pair not being detected, as is the case in path groups A  
 678 and B. Additionally, there is ambiguity in the position of the second-to-last  
 679 post/trunk pair because vines have been planted in close proximity to the  
 680 posts. Analysis of the recorded sensor data shows this to be the cause of the  
 681 separation in end-positions between points A and B.

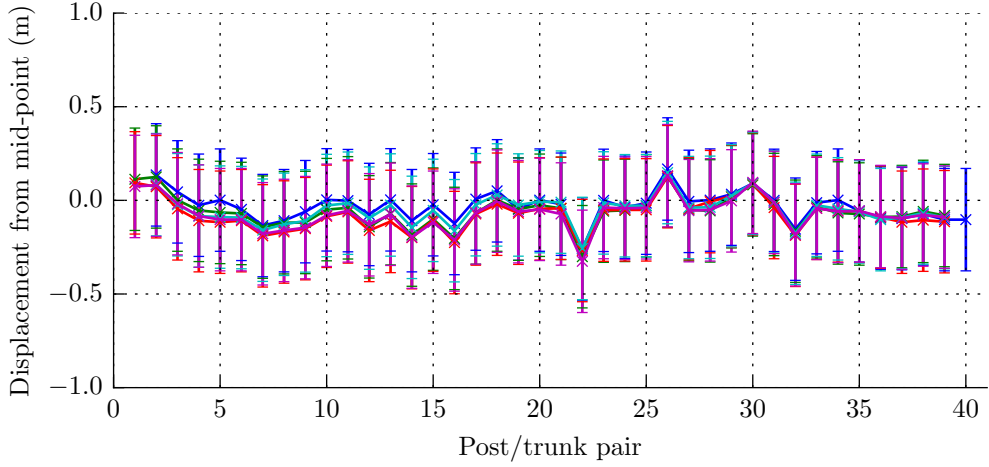


Figure 17: Deviation between vehicle’s tracking point and each post/trunk pair midpoint over five trials. The mean row width was 4.35 m.

## 682 7. Discussion

683 The reported platform meets the previously specified requirements and  
 684 has proved its usefulness during three pollination and harvesting seasons.  
 685 However, during these operations the vehicle was operated under manual  
 686 control because of the need to drive close to row boundaries. The width of the  
 687 vehicle and modules meant it was necessary to perform two passes through  
 688 each row in order to access the full canopy area. The vehicle’s overall height  
 689 is 1.25 m, leaving 0.15 m between it and the target ceiling height of 1.4 m.

690 Results from navigation tests indicate that multi-layer lidar with wheel  
 691 encoder feedback are sufficient for row turning tasks. For row following,  
 692 an IMU and multi-layer lidar based algorithm produced paths which were  
 693 sufficiently repeatable and close to the row’s centre-line. Wheel slippage  
 694 meant that the encoder information from driven wheels was less suitable for  
 695 long-term odometry than the odometry information provided by the SLAM  
 696 package, which was based on processed lidar and IMU data. Future work  
 697 will combine the lidar, IMU, and encoder based odometry outputs into a sin-  
 698 gle output for longer term accuracy. The method for turning between rows  
 699 calls for further work. Row end turning was a manual process that involved  
 700 observing an autonomously driven turn and manually adjusting the length  
 701 or radius of the turn’s segments. Future work will focus on enabling the

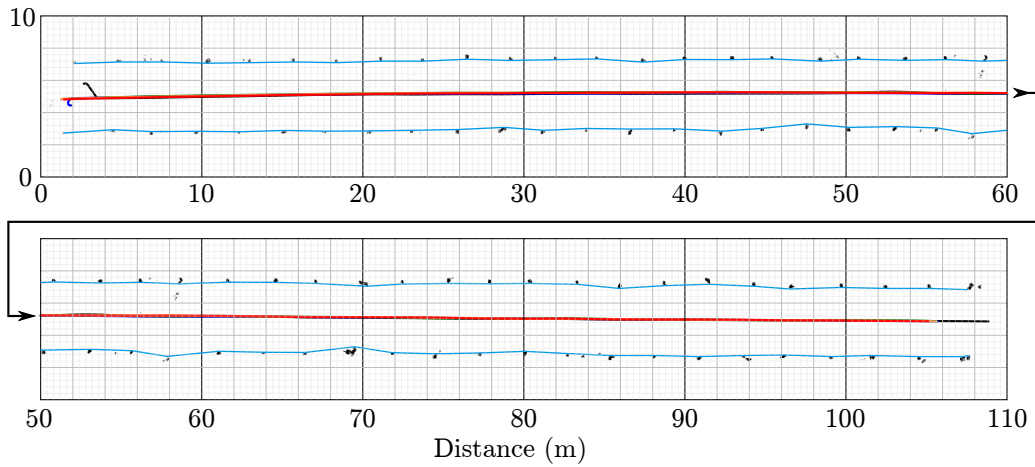


Figure 18: Row-following paths shown relative to row boundaries. Boundary lines are linked with blue lines.

702 system to plan row-end turns based on sensor data – without a manually  
 703 created map. Observationally, detecting row end-points based on the vehicle’s proximity to the last post-pair proved more reliable than detecting the  
 704 presence/absence of canopy.  
 705

706 The platform’s 96 V battery pack and electrical system introduced a elec-  
 707 trical hazard during development. The authors suggest a voltage of 48 V as  
 708 it bears a reduced risk of injury from shock. Inputs of 48 V are supported  
 709 across a wider range of motors, motor controllers, and power converters, but  
 710 cabling requirements are increased.

711 The series-hybrid configuration allowed the vehicle to drive and provide  
 712 power to subsystems without running the petrol engine. This was useful  
 713 in testing scenarios, where people are in close proximity to the vehicle, as it  
 714 eliminated exhaust fumes and reduced noise and vibration. However, robotic  
 715 modules and the bin-lifting mechanism required pneumatic pressure to func-  
 716 tion. As the air-compressor was belt driven from the petrol engine it was  
 717 necessary to frequently run the engine. An electric air-compressor would  
 718 allow the system to run without the petrol engine for much longer periods.

719 The use of more general purpose platforms to test navigation algorithms  
 720 enabled the navigation system to be developed in parallel with the physical  
 721 hardware. Their smaller size eliminated the risk of serious injury and led to a  
 722 speed up in development and test cycles. It also meant that navigation testing  
 723 could continue while the full-size platform was engaged in other activities.

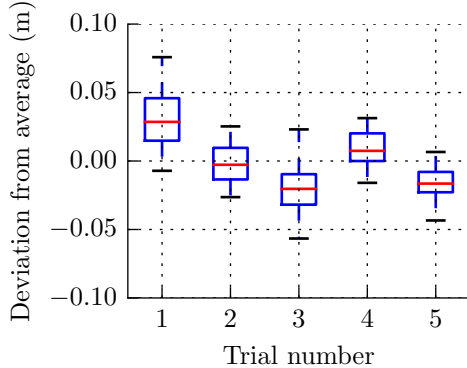


Figure 19: Repeatability analysis of five row-following trials. Whiskers represent maximum deviations in both the positive and negative directions. Each trial has a sample size of 40.

## 724 8. Conclusion

725 This work presents a platform designed specifically for autonomously  
 726 transporting task-specific modules through pergola-style kiwifruit orchards.  
 727 The platform proved capable of carrying over twice the mass of similar plat-  
 728 forms reported previously. The four wheel drive system with two individually-  
 729 actuated steering wheels proved to be well suited for use in and around  
 730 kiwifruit orchards. The authors deem the use of a four-wheel steering con-  
 731 figuration in this environment to be unnecessary.

732 Various navigation sensors were trialled in the kiwifruit orchard environ-  
 733 ment. Multi-layer lidar proved to be the most versatile sensor for orchard  
 734 based navigation owing to its wide field-of-view and robust outputs. Using  
 735 a map of manually adjusted row-end turns, the platform has navigated over  
 736 10 km of orchard blocks using only wheel-encoders and a single multi-layer  
 737 lidar. A significant amount of work was required to tune the row-end-turns,  
 738 which has implications for commercial deployment. Row following tests us-  
 739 ing an algorithm based only on multi-layer lidar and IMU inputs proved to  
 740 be repeatable to within  $\pm 75$  mm.

741 The use of smaller, commercially available, robots proved valuable when  
 742 developing navigation software due to their safety and portability. Future  
 743 work will focus on developing the navigation system so that the vehicle can  
 744 plan row-end turns and avoid obstacles whilst row following.

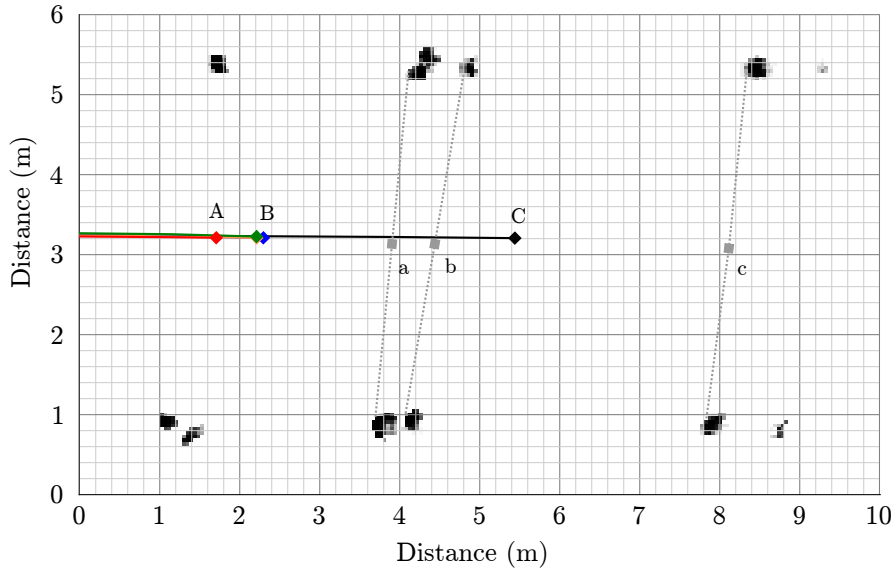


Figure 20: Graph showing row-following end positions relative to tracked row features. Grey dotted lines connect row feature pairs, with squares indicating their mid-points.

#### 745 Acknowledgements

746 This research was supported by the New Zealand Ministry for Business,  
 747 Innovation and Employment (MBIE) on contract UOAX1414. The authors  
 748 acknowledge contributions from Phillip Ross, Gordon Neshausen, Josh Bar-  
 749 nett, and Erin Simms who were involved with design and fabrication.

#### 750 References

- 751 Åstrand, B., & Baerveldt, A. J. (2002). An agricultural mobile robot with  
 752 vision-based perception for mechanical weed control. *Autonomous Robots*,  
 753 13, 21–35.
- 754 Bak, T., & Jakobsen, H. (2004). Agricultural Robotic Platform with Four  
 755 Wheel Steering for Weed Detection. *o*, 87, 125–136.
- 756 Bawden, O., Kulk, J., Russell, R., Mccool, C., English, A., Dayoub, F.,  
 757 Lehnert, C., & Perez, T. (2017). Robot for weed species plant-specific  
 758 management. *Journal of Field Robotics*, (pp. 1–21).

- 759 Bell, J., MacDonald, B. A., & Ahn, H. S. (2016). Row following in per-  
760 gola structured orchards. In *2016 IEEE/RSJ International Conference on*  
761 *Intelligent Robots and Systems (IROS)* (pp. 640–645).
- 762 Bell, J., Macdonald, B. A., & Ahn, H. S. (2017). Row Following in Pergola  
763 Structured Orchards by a Monocular Camera Using a Fully Convolutional  
764 Neural Network. In *Australasian Conference on Robotics and Automation*  
765 (*ACRA*).
- 766 Hess, W., Kohler, D., Rapp, H., & Andor, D. (2016). Real-time loop closure  
767 in 2D LIDAR SLAM. In *Proceedings - IEEE International Conference on*  
768 *Robotics and Automation*.
- 769 Klose, R., Thiel, M., Ruckelshausen, a., & Marquering, J. (2008). Weedy  
770 – a sensor fusion based autonomous field robot for selective weed control.  
771 *Land. Technik 2008, 2045*, 167–172.
- 772 Li, M., Imou, K., Wakabayashi, K., & Yokoyama, S. (2009). Review of re-  
773 search on agricultural vehicle autonomous guidance. *International Journal*  
774 *of Agricultural and Biological Engineering, 2*, 1–16.
- 775 Pedersen, T. S., Nielsen, K. M., Andersen, P., & Nielsen, J. D. (2002). Devel-  
776 opment of an Autonomous Vehicle for Weed and Crop Registration. *Inter-*  
777 *national Conference on Agricultural Engineering AgEng2002, Budapest,*.
- 778 Robert Bosch GmbH (2002). *Electronic Automotive Handbook*. (1st ed.).
- 779 Ruckelshausen, A., Biber, P., Dorna, M., Gremmes, H., Klose, R., Linz,  
780 A., Rahe, F., Resch, R., Thiel, M., Trautz, D., Weiss, U., Doma, M., &  
781 Rahne, R. (2009). BoniRob: an autonomous field robot platform for indi-  
782 vidual plant phenotyping. *Proceedings of Joint International Agricultural*  
783 *Conference (2009), 9*, 841–847.
- 784 Scarfe, A. J. (2012). *Development of an Autonomous Kiwifruit Harvester*.  
785 Doctoral dissertation Massey University, Palmerston North, New Zealand.
- 786 Scarfe, A. J., Flemmer, R. C., Bakker, H. H., & Flemmer, C. L. (2009).  
787 Development of an autonomous kiwifruit picking robot. In *Autonomous*  
788 *Robots and Agents, 2009. ICARA 2009. 4th International Conference on*  
789 (pp. 380–384). IEEE.

- 790 Slaughter, D. C., Giles, D. K., & Downey, D. (2008). Autonomous robotic  
791 weed control systems: A review. *Computers and Electronics in Agriculture*,  
792 61, 63–78.
- 793 Statistics New Zealand (2015). Annual Fruit Exports Hit \$2 Billion for First  
794 Time.
- 795 Tillett, N. D., Hague, T., & Marchant, J. A. (1998). A Robotic System for  
796 Plant-Scale Husbandry. *Journal of Agricultural Engineering Research*, 69,  
797 169–178.
- 798 Timmins, J. (2009). Seasonal Employment Patterns in the Horticultural  
799 Industry.